nature communications

Article

https://doi.org/10.1038/s41467-024-54288-w

Ultrafast bounce of particle-laden droplets

Received: 12 June 2024

Accepted: 5 November 2024

Published online: 16 November 2024

Check for updates

Yanhong Li[1], Wenchang Zhao[1], Ying Zhou[1], Shuxian Tang[1], Shiyu Wang[1], Yutong Zheng[1], Zuankai Wang[2] ✉ & Pingan Zhu[1,3] ✉

The rebound of liquid droplets on solid surfaces exhibits behavior reminiscent of elastic spheres, albeit with distinct contact dynamics. While the rapid detachment of droplets from surfaces holds significant relevance for various applications, previous endeavors relying on engineered surfaces can only reduce the contact time to several milliseconds, primarily due to capillary effects dominating droplet bounce. Here, we present ultrafast rebound by designing heterogeneous core-shell droplets encapsulating a particle (DEP), which achieves an unprecedentedly short contact time of 0.3 ms and 0.05 ms with polydimethylsiloxane and glass particles, respectively. This remarkable contact-time reduction is universally applicable to diverse systems, including both water and oil droplets, elastic and rigid particles, super-repellent and superlyophilic surfaces, and is effective across a wide range of impact velocities. Beyond exhibiting liquid-like dynamics, DEP manifests solid-like behavior owing to asynchronized motions between the particle and the droplet, which effectively breaks down the dominance of capillarity. With systematic experimental and analytical studies, we delineate contact times in three bouncing regimes and identify critical conditions governing regime transitions. DEP amalgamates the bouncing dynamics of both solids and liquids, offering a robust and versatile strategy for tailoring contact time to suit diverse applications involving solid-liquid composite systems.

In contemplating the graceful dance and subsequent rebound of a raindrop on a superhydrophobic lotus leaf, one uncovers a process of droplet impact that transcends our immediate perception. This phenomenon, initially explored by Worthington in 1876 through the analysis of patterns left on smoked glass plates[1], has evolved into a profound understanding of droplet-surface interactions[2–5]. At the crux of this process lies the "contact time" (t_c), a defining timescale governing the intricate dynamics of mass, momentum, and energy transfer during the contact between droplets and surfaces. This temporal parameter, crucial in various applications such as anti-icing[6,7], anti-fogging[8], self-cleaning[9–11], electricity generation[12,13], heat transfer[14,15], and liquid transport[16], has garnered escalating interest over the past two decades. While strategies for prolonging contact time, such as employing adhesive surfaces to impede droplet motion[17,18], are relatively straightforward, achieving a reduction in contact time necessitates a more judicious design.

For inviscid droplets impacting super-repellent surfaces with minimal energy dissipation[16,19–21], the interplay between inertia and capillarity governs the contact time[22]. This relationship is expressed by the inertial-capillary timescale $\tau = \sqrt{\rho R_0^3/\gamma}$, with $t_c = (\pi/\sqrt{2})\tau$, where ρ, R_0, and γ denote the density, radius, and surface tension of the droplet[2,23]. The theoretical ratio of $\pi/\sqrt{2} \approx 2.2$, derived from the lowest-order oscillation period of a spherical droplet by Rayleigh[24], establishes the typical contact time for millimeter-sized droplets at around ten milliseconds. Various endeavors within the inertial-capillary framework have focused on reducing the time ratio by modulating droplet-bouncing dynamics. This includes engineering surfaces with macroscopic ridges[25–30], submillimeter posts[31–34], macroscale curvatures[30,35–37], compact nanoscale textures[38], substrate elasticity[39,40], and dynamic motions[41,42]. Despite these commendable

[1]Department of Mechanical Engineering, City University of Hong Kong, 999077 Hong Kong, China. [2]Department of Mechanical Engineering, Hong Kong Polytechnic University, 999077 Hong Kong, China. [3]Shenzhen Research Institute, City University of Hong Kong, 518057 Shenzhen, China.
✉e-mail: zk.wang@polyu.edu.hk; pingazhu@cityu.edu.hk

endeavors, the contact time remains primarily determined by capillarity, thereby limiting it to be above several milliseconds. Breaking this theoretical constraint to further reduce the contact time appears challenging, if not impossible.

To circumvent this grand challenge, our focus shifts to tuning droplet heterogeneity rather than engineering solid surfaces for customizable bouncing dynamics. Employing core-shell droplets encapsulating a particle (DEP), we unveil ultrafast bouncing behavior with an unprecedentedly short contact time of 0.3 ms and 0.05 ms using elastic and rigid particles, respectively. Such minimum contact time occurs at relatively low impact velocities, where the bouncing dynamics of DEP are predominantly dictated by the particle, rather than the droplet shell. Consequently, the contact time becomes independent of surface tension but relies on the impact velocity, thereby transcending the confines of the inertial-capillary timescale. As impact velocity increases beyond a certain threshold, both the particle and the droplet shell govern the bouncing dynamics, leading to a linear increase in contact time with impact velocity. Eventually, contact time approaches a constant value dictated by capillarity as impact velocity exceeds another critical threshold, diminishing the influence of the particle. Throughout all regimes, the contact time of DEP remains significantly reduced.

Results

Ultrafast rebound of DEP

Figure 1 delineates the distinctive bouncing dynamics observed in the impact of a DEP (Fig. 1a), a liquid droplet (Fig. 1b), and a solid particle (Fig. 1c), all subjected to an identical impact velocity of $V = 0.455\ \mathrm{m\ s^{-1}}$ and possessing a radius of $R_0 \approx 0.81$ mm. The core-shell DEP is composed of polydimethylsiloxane (PDMS) as the particle and silicone oil (surface tension $\gamma = 19.15\ \mathrm{mN\ m^{-1}}$, viscosity $\mu = 18.5$ mPa·s) as the droplet shell. This choice is rooted in the favorable super-spreading characteristics of silicone oil on the PDMS surface, manifesting very small contact angles (Supplementary Fig. 1 and Supplementary Table 1). The density of the PDMS particle (ρ_p, see Supplementary Table 2), slightly surpassing that of silicone oil ($\rho_l = 949.9\ \mathrm{kg\ m^{-3}}$), ensures the proximity of the particle to the base of the DEP (Fig. 1a). The controlled release of DEP from an adjustable height enables a precisely regulated impact velocity (V), followed by its descent onto a superamphiphobic surface (Supplementary Fig. 2). Controlling the particle's radius (R_p) and the DEP's radius (R_0) enables the tunability of the particle's volume fraction, $\Phi = (R_p/R_0)^3$. For a fair comparison, the liquid droplet (Fig. 1b) is composed of silicone oil, and the solid particle (Fig. 1c) is fabricated using PDMS, representing extreme cases of $\Phi = 0$ and $\Phi = 1$, respectively. With the introduction of Φ, the effective density of DEP (ρ_e) is defined as $\rho_e = \Phi\rho_p + (1-\Phi)\rho_l$.

The DEP exhibits a remarkably swift detachment from the surface within a much short period of 0.3 ms (Fig. 1a), showcasing ultrafast bouncing behavior akin to that of the solid particle (Fig. 1c, $t_c = 0.3$ ms), but markedly distinct from the liquid droplet (Fig. 1b, $t_c = 10.8$ ms). Both the DEP and the solid particle display significantly reduced deformation and shorter contact time in contrast to the droplet (Supplementary Movie 1). Markedly, the DEP's contact time ratio manifests $t_c/\tau = 0.057$ ($\tau = 5.23$ ms with $\tau = \sqrt{\rho_e R_0^3/\gamma}$), signifying an unprecedented 97% reduction. It is noteworthy that the ultrafast bouncing of DEP is universal across diverse systems. This phenomenon is also observed when an aqueous droplet encapsulating an elastic hydrogel particle (Supplementary Fig. 3 and Supplementary Movie 2), a water-PDMS Janus structure (Supplementary Fig. 4 and Supplementary Movie 2), and a silicone oil droplet encapsulating a rigid glass particle (Supplementary Fig. 5 and Supplementary Movie 2) impacts various surfaces, including glass, aluminum, and polytetrafluoroethylene (PTFE) substrates (Supplementary Fig. 6 and Supplementary Movie 2).

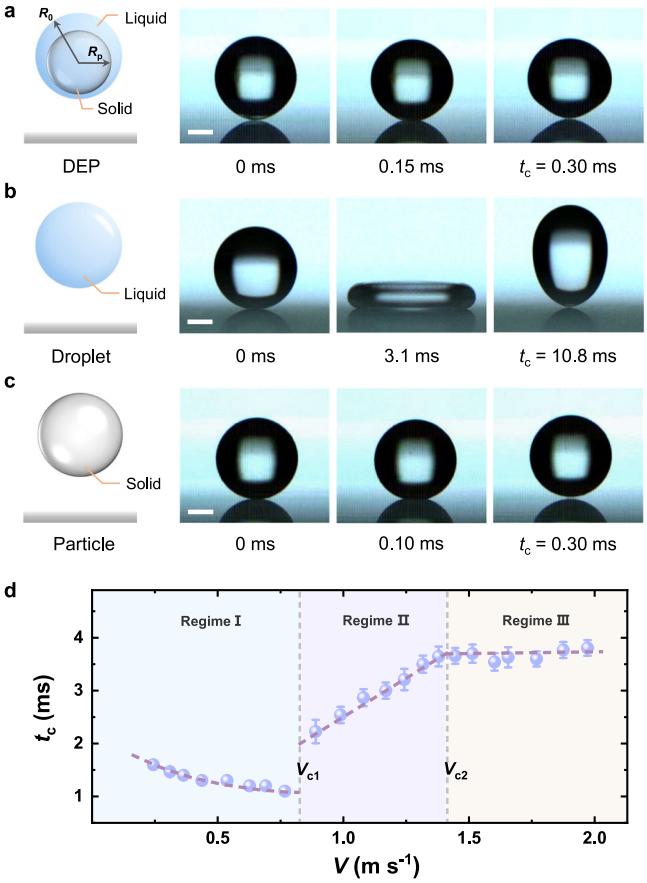

Fig. 1 | Contrast in the bouncing behavior of different systems. a–c Schematics and snapshots depicting bouncing dynamics of a droplet encapsulating a particle (DEP), a liquid droplet, and a solid particle, respectively, under an impact velocity of 0.455 m s^{-1}. The particle volume fraction (Φ) is 49.3%. The Young's modulus of the PDMS particle is 220.9 kPa. The contact time (t_c) is 0.3 ms for DEP, 10.8 ms for the droplet, and 0.3 ms for the particle. Scale bar, 0.5 mm. **d** Variation of contact time with increasing impact velocity for a DEP ($\Phi = 50.1\%$). Three distinct regimes are identified as impact velocity increases. The Young's modulus of the PDMS particle is 10.4 kPa.

The contact time of DEP varies distinctly with increasing impact velocity (V), revealing three regimes (Fig. 1d). In regime I, where $V < V_{c1}$ (with V_{c1} as a critical velocity), t_c gradually decreases with increasing V. In regime II, where $V_{c1} < V < V_{c2}$ (with V_{c2} as another critical velocity), t_c exhibits a linear increase with V. In regime III, where $V > V_{c2}$, t_c remains nearly constant. This unique dependence of t_c on V for DEP contrasts sharply with liquid droplets, where t_c remains independent of V. Moreover, the contact time of DEP is significantly shorter than that of liquid droplets (approximately ten milliseconds) across all three regimes, indicating that the inclusion of a particle within the droplet fundamentally alters the bouncing dynamics.

Hertz regime

To unravel the intricacies of the ultrafast bouncing exhibited by DEP in Regime I, a detailed investigation into its morphological transformations during impact is imperative, as illustrated in Fig. 2a. During the spreading stage, the particle core and the droplet shell undergo a coherent deformation, maintaining their integrity. However, a noteworthy asynchronization becomes apparent during the receding stage, marked by the separation of the core and shell at the bottom of the DEP. Remarkably, the DEP assumes a helmet shape that remains nearly invariant even after takeoff (3.25 ms, Fig. 2a), presenting a stark departure from the oscillating shape exhibited by a bouncing droplet (Supplementary Movie 3).

https://doi.org/10.1038/s41467-024-54288-w

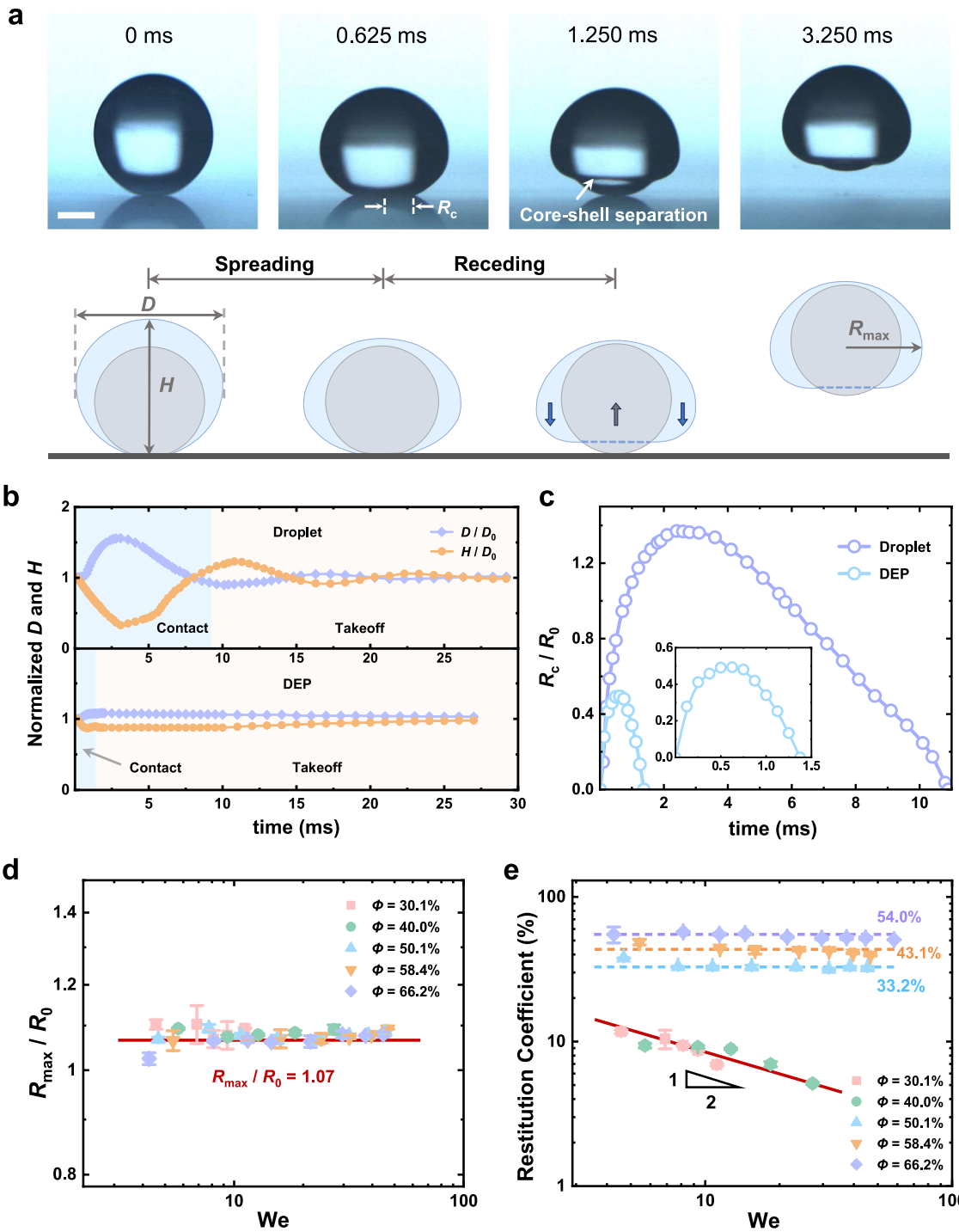

Fig. 2 | Bouncing dynamics of DEP in the Hertz regime. a Snapshots and schematics of DEP during impact at $\Phi = 49.5\%$ and $V = 0.443$ m s^{-1}. Scale bar, 0.5 mm. The core-shell separation occurs due to asynchronized motions between the core and the shell (indicated by arrow) during receding, resulting in DEP adopting a helmet shape. **b** Morphological changes of a droplet and a DEP over time. The diameter D and height H are normalized by the initial diameter $D_0 = 2R_0$. **c** Evolution of contact radius (R_c) normalized by the initial radius (R_0) for a DEP and a liquid droplet. **d** The plot of the maximum deformation radius (R_{max}, normalized by R_0) of DEP during impact under different volume fractions (Φ) and Weber numbers (We). **e** The plot of the restitution coefficient of DEP under different Φ and We.

This distinction is further evidenced by the temporal variations in the diameter (D) and height (H) of the two systems (Fig. 2b). Figure 2c shows the dynamic evolution of the contact radius (R_c) for both DEP and a liquid droplet. The liquid droplet exhibits a typical two-stage variation in R_c: it spreads with a $t^{1/2}$ dependency during spreading and decreases linearly with time (t) during receding. In contrast, the DEP demonstrates a more symmetric deformation over time. The maximal deformation of the DEP is notably smaller than that of the liquid droplet, which greatly contributes to the reduction in both spreading and receding times, ultimately leading to a decreased contact time. These findings underscore the distinct bouncing dynamics of DEP compared to liquid droplets.

The core-shell separation stems from the core particle rebounding much more rapidly than the droplet shell. Consequently, as the particle begins its upward motion during receding, the majority of the droplet shell fails to make contact with the bottom surface

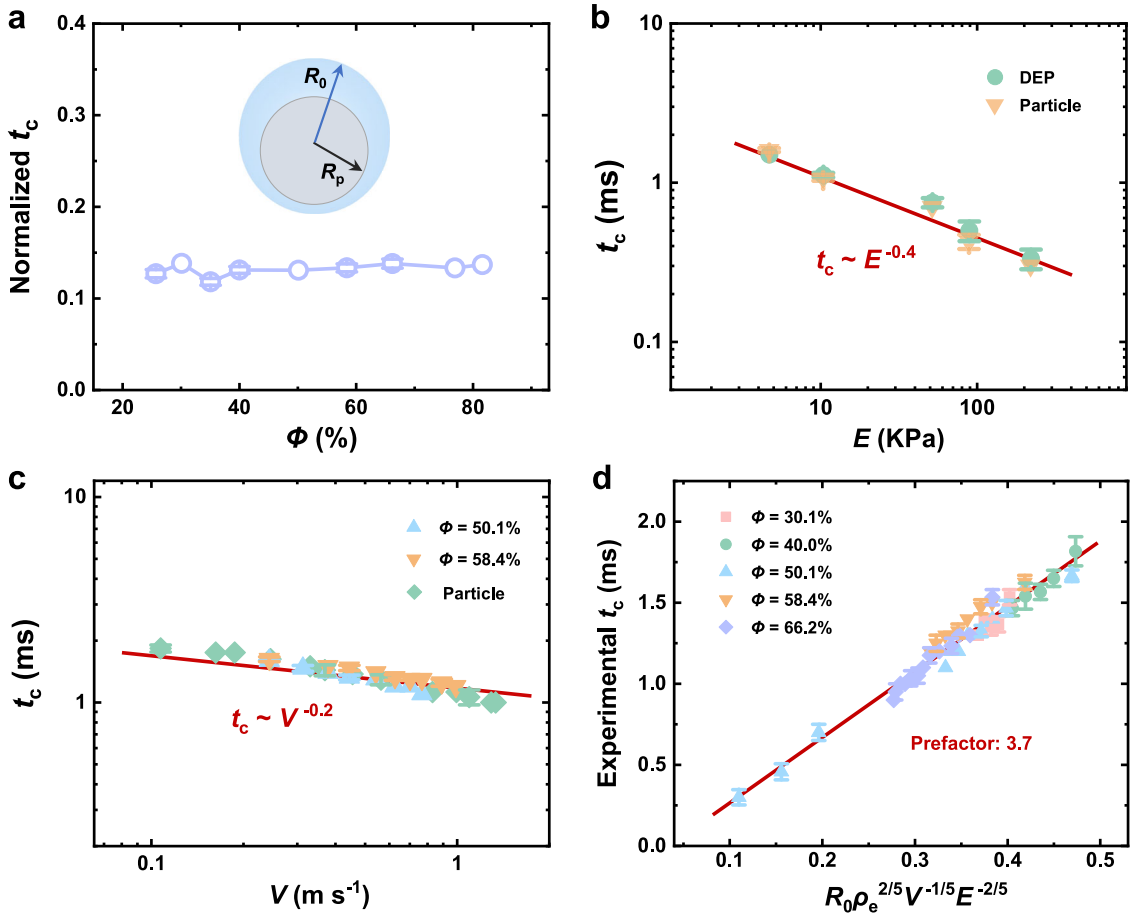

Fig. 3 | Contact time of DEP in the Hertz regime. a The dependence of contact time on the volume fraction of DEP. The contact time (t_c) of the DEP is normalized by that of the droplet with the same size. The impact velocity is 0.236 m s^{-1}. **b** The relationship between contact time (t_c) and Young's modulus (E) of the particle. Both the DEP (Φ = 48.8%) and the pristine particle display nearly identical contact times with the same scaling of $t_c \sim E^{-0.4}$. The impact velocity of both systems is 0.445 m s^{-1}. **c** The correlation between contact time (t_c) and impact velocity (V) for both DEP and pristine particle. All data collapse onto a single master curve with a scaling of $t_c \sim V^{-0.2}$. **d** Comparison of experimental results and theoretical predictions of the contact time of DEP. The theoretical values are calculated using Eq. (1).

while retaining a downward velocity. This velocity mismatch propels the particle upward to the upper part of the shell, inducing the observed separation. Hence, the overall bouncing behavior of DEP is decisively influenced by the localized dynamics of the core particle.

Notably, the maximum deformation factor (R_{max}/R_0) for the DEP is found to be independent of both the particle volume fraction and the impact Weber number ($We = 2\rho_l V^2 R_0/\gamma$). It maintains a constant value of around 1.07, indicating minimal deformation (Fig. 2d), reminiscent of impacting elastic particles (Supplementary Fig. 7a). In stark contrast, impacting droplets exhibit Reynolds number ($Re = 2\rho_l V R_0/\mu$) dependent deformation, with R_{max}/R_0-$Re^{1/4}$ (Supplementary Fig. 7b). This scaling can be attributed to the transfer of kinetic energy to surface energy and viscous dissipation[17].

The restitution coefficient ($\varepsilon = V_{reb}/V$, with V_{reb} denoting the rebound velocity) for the DEP remains independent of We for $\Phi > 50\%$ (Fig. 2e), mirroring the bouncing dynamics of the particles where ε is unaffected by impact velocity (Supplementary Fig. 7c). The increase in ε with Φ signifies the enhanced dominance of the particle in DEP. Conversely, for DEP with $\Phi < 50\%$, ε exhibits a dependence on We, following $\varepsilon \sim We^{-1/2}$ (Fig. 2e). This scaling law aligns with that observed in impacting droplets (Supplementary Fig. 7d), emanating from a constant rebound velocity[19]. Consequently, we establish that DEP with $\Phi > 50\%$ manifests a complete solid-like bouncing behavior and $25.7\% < \Phi < 50\%$ demonstrates partial solid-like behavior. Further decreasing Φ will cause DEP to approach a liquid-like state, resulting in similar bouncing behaviors and comparable contact times to liquid droplets (Supplementary Fig. 8 and Supplementary Movie 4). Therefore, maintaining a Φ value above 25% is optimal for achieving distinct bouncing dynamics of DEP in this study.

To scrutinize the influence of solid-like behavior on the contact time of the DEP, we explore the dependence of t_c on various parameters. Intriguingly, once the DEP adopts solid-like bouncing dynamics, the contact time proves to be nearly independent of the particle volume fraction (Fig. 3a). This characteristic endows significant flexibility in tuning t_c without the necessity of meticulously selecting Φ. The solid-like behavior is anticipated to be influenced by factors such as the Young's modulus (E) of the particle (Supplementary Fig. 9 and Supplementary Table 2) and impact velocity. We reveal scaling laws of $t_c \sim E^{-0.4}$ (Fig. 3b) and $t_c \sim V^{-0.2}$ (Fig. 3c) for both the DEP and solid particles. These scaling laws manifest fundamental deviations from the scaling of the inertial-capillary timescale for droplets (Supplementary Fig. 10), thus disrupting the dominance of capillarity.

The congruence in scaling laws between DEP and solid particles evokes parallels with the Hertz contact theory[2,5], which is applicable under conditions of slight deformation (Fig. 2c and Supplementary Fig. 7a). Accordingly, we postulate (Supplementary Note 1):

$$t_c \sim R_0 \rho_e^{2/5} V^{-1/5} E^{-2/5} \quad (1)$$

Equation (1) aligns seamlessly with the experimental results of the two scaling laws in Fig. 3b, c. The theoretical predictions of t_c using Eq. (1) are depicted in Fig. 3d, illustrating a remarkable agreement with the experimental data by introducing an empirical prefactor of 3.7.

Consequently, the solid-like bouncing behavior of DEP finds apt description within the Hertz contact theory, and we designate this regime as the "Hertz regime". Based on this scaling law, it is anticipated that incorporating a rigid particle with a higher Young's modulus will further reduce the contact time of DEP. For instance, t_c can reach 0.05 ms when a glass particle is encapsulated in a silicone oil droplet (Supplementary Fig. 5 and Supplementary Movie 2).

It is noteworthy that the radius of DEP (R_0), rather than the particle radius (R_p), is employed in Eq. (1) for theoretical predictions. This revelation underscores that the inclusion of only a small portion of the solid particle (Φ as small as 25.7% in experiments) into droplets can transform the bouncing dynamics of the entire DEP from liquid-like to solid-like, effectively transcending the influence of capillarity. Given that the particle exclusively governs the DEP's deformation at the bottom in contact with the surface, this observation emphasizes the paramount importance of local contact dynamics in dictating the overall bouncing behavior.

Partial retraction regime

At elevated impact velocities, the droplet shell can contact the solid surface, undergoing spreading and receding processes (Fig. 4a and Supplementary Movie 5). This results in an elongated contact time in Regime II compared to DEP in the Hertz regime (Regime I). Despite this transition, the encapsulated particle continues to influence the overall bouncing dynamics.

After impact, the deformation and rebound of the particle occur rapidly within the spreading of the droplet shell (0–1.0 ms, Fig. 4a). Upon takeoff, the particle restores its spherical shape and halts the spreading of the droplet shell (1.0 ms, Fig. 4a). Consequently, the droplet shell is compelled to recede in conjunction with the particle's upward movement (1.7 ms, Fig. 4a). As the particle leads the droplet shell during bouncing, this asynchronous motion results in an elongated shape of the droplet shell and a noticeable separation between the particle and the droplet shell, creating a void within the DEP (1.7–2.5 ms, Fig. 4a). Thus, the morphological change of DEP in this regime is more pronounced than in the Hertz regime, while DEP still exhibits fewer shape oscillations and deformations than the liquid droplet due to the particle encapsulation (Fig. 4b).

A remarkable characteristic of bouncing DEP is the early takeoff of the droplet shell, marked by a flat bottom surface with a non-zero contact radius at takeoff (R_{ct}), where the retraction process remains incomplete (Fig. 4a and c). Therefore, we refer to Regime II as the "partial retraction regime". The rapid bouncing of the particle reduces the maximum spreading of the droplet shell and results in incomplete retraction, collectively leading to a substantial reduction in the contact time of DEP (Fig. 4c). Notably, the contact radius recedes linearly with time for DEP before reaching R_{ct}, indicating a constant retraction velocity (V_r), distinct from the retraction observed in the Hertz regime. Interestingly, we find that V_r for DEP is dictated by the takeoff velocity (V_p) of the particle (Fig. 4d), suggesting that the early takeoff of the droplet shell is governed by the kinetics of the bouncing particle.

Figure 4e demonstrates that the normalized R_{ct} decreases almost linearly with impact velocity V, such that $R_{ct}/R_{cm} \propto -V$, where R_{cm} indicates the maximum contact radius. As V increases, the droplet shell gains greater impacting kinetic energy, enhancing the hydrodynamic effects that favor complete retraction, while competing with the particle's lift-up effect that induces the early takeoff of the droplet shell. Consequently, R_{ct} decreases with V, leading to an increased retraction length ($R_{cm} - R_{ct}$), which is responsible for an increase in contact time (Fig. 4f). Assuming a constant contact time that scales as τ if the droplet shell can fully retract, the contact time in the partial retraction regime becomes proportional to $(R_{cm} - R_{ct})\tau/R_{cm}$, yielding $t_c \sim (1 - R_{ct}/R_{cm})\tau \propto -R_{ct}/R_{cm} \propto V$. Thus, in this regime, contact time is proportional to the impact velocity V (Fig. 4f). These results indicate that the bouncing dynamics of DEP in the partial retraction regime are concurrently influenced by both the particle and the droplet shell.

Complete retraction regime

As the impact velocity exceeds a critical value, the particle achieves a sufficient takeoff velocity, allowing it to separate rapidly from the droplet shell, resulting in a more elongated DEP shape at takeoff (Fig. 5a and Supplementary Movie 6). Under this condition, the retraction of the droplet shell is no longer influenced by the particle with R_{ct} reducing to zero. This transition indicates a shift in the bouncing dynamics of DEP from the partial retraction regime to the "complete retraction regime." In this regime, the spreading process of DEP resembles that in the partial retraction regime, and the shape of DEP exhibits reduced oscillations and deformations compared to the liquid droplet (Fig. 5b, c). However, complete retraction of the droplet shell signifies that hydrodynamic effect dominates over the particle's kinetic effect.

The diminishing influence of the particle on retraction is evident in the differences between V_p and V_r, with V_p increasing linearly with V while V_r remains constant at approximately 0.8 m s^{-1} (Fig. 5d). Consequently, the retraction Reynolds number ($\mathrm{Re} = \rho_l V_r h/\mu$) is calculated as $\mathrm{Re} \approx 4.1 \sim O(1)$ by using $\rho_l = 949.9$ kg m^{-3}, $V_r = 0.8$ m s^{-1}, $\mu = 18.5$ mPa·s, and h as the thickness of the receding liquid film, characterized by a height of ~100 μm. Thus, the retraction velocity results from a balance among capillary pressure, viscous stress, and fluid inertia: $\gamma/h \sim \rho_l V_r^2 \sim \mu V_r/h$. This scaling argument predicts a constant value of $V_r \sim \gamma/\mu \sim 1.04$ m s^{-1} ($\gamma = 19.15$ mN s^{-1}), aligning closely with the experimental value of $V_r = 0.8$ m s^{-1}.

In the complete retraction regime, contact time is solely determined by the droplet shell with a mass of $\rho_l R_0^3(1-\Phi)$, scaling with the natural oscillation time as $t_c \sim \sqrt{\rho_l R_0^3(1-\Phi)/\gamma} \sim \sqrt{(1-\Phi)}\tau_l$, where $\tau_l = \sqrt{\rho_l R_0^3/\gamma}$. Therefore, the normalized contact time is a function of volume fraction,

$$t_c/\tau_l \sim \sqrt{(1-\Phi)} \tag{2}$$

As shown in Fig. 5e, this prediction shows good agreement with experimental results.

It is important to note that the three regimes are identified under the condition that the particle resides at the bottom of the DEP due to its higher density compared to the liquid ($\rho_p > \rho_l$). However, when $\rho_p < \rho_l$, the particle will position itself at the top, allowing the bottom droplet shell to make direct contact with the solid surface upon impact. Consequently, DEP immediately enters the complete retraction regime, regardless of impact velocity (Supplementary Fig. 11 and Supplementary Movie 7). In this scenario, the contact time of DEP reaches a constant value that remains substantially shorter than that of a liquid droplet (Supplementary Fig. 11).

Transition diagram

The transitions between the three regimes are delineated by two critical velocities, V_{c1} and V_{c2} (Fig. 1d). The transition from the Hertz regime to the partial retraction regime occurs concurrently with the shift from particle-surface to liquid-surface contacts. Achieving this transition necessitates that the droplet shell must attain the critical impact velocity V_{c1} to descend onto the surface, which increases with the particle volume fraction (Supplementary Fig. 12a). From an energy perspective, the kinetic energy of the droplet shell ($\sim \rho_l R_0^3(1-\Phi)V^2$) must overcome the penalty associated with the increase in surface energy due to surface deformation ($\sim \gamma R_0^2$). The balance between these two energies gives rise to a critical condition for the transition:

$$\mathrm{We} \sim (1-\Phi)^{-1} \tag{3}$$

https://doi.org/10.1038/s41467-024-54288-w

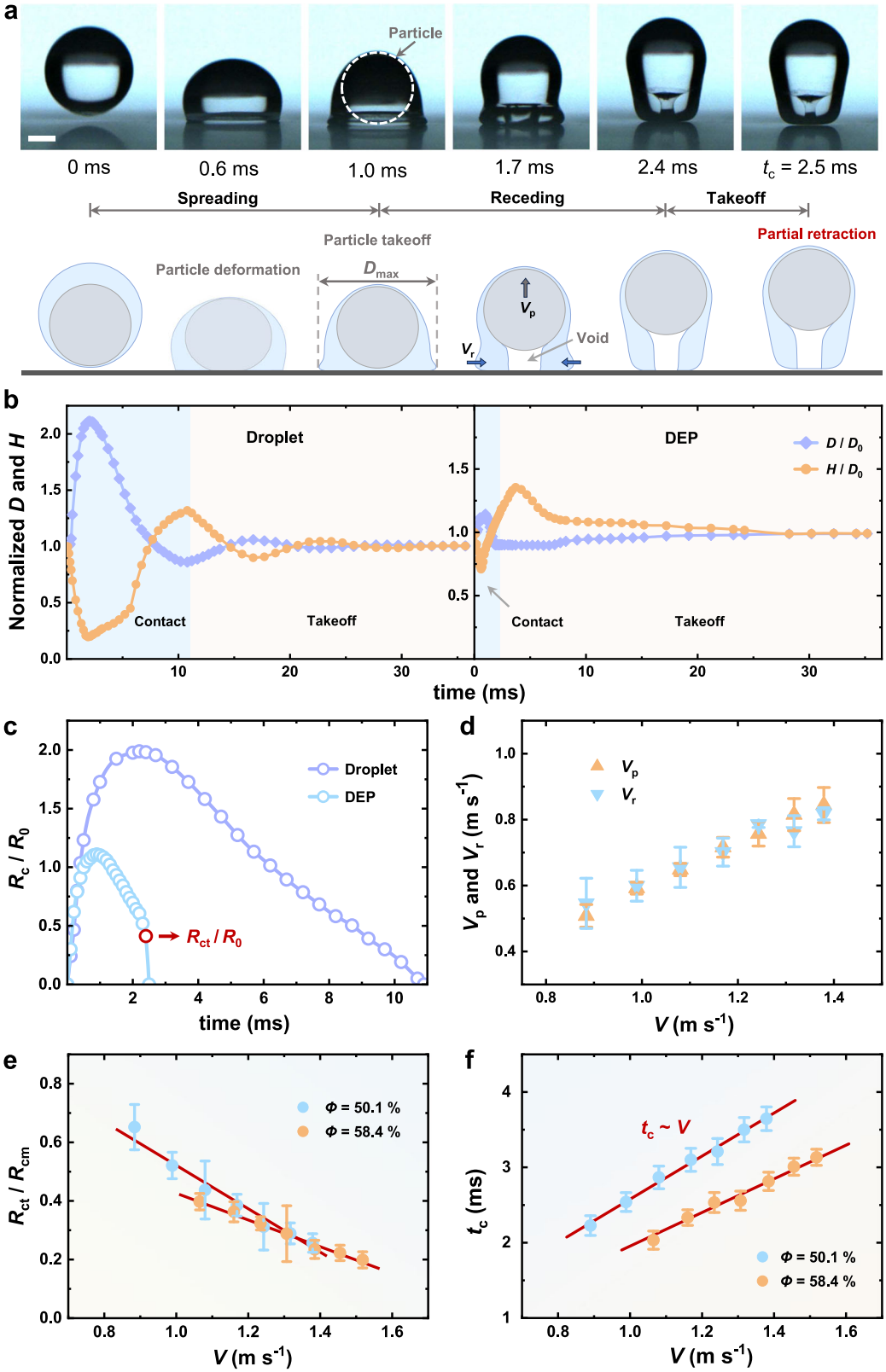

Fig. 4 | Partial retraction of DEP. a Snapshots and schematics illustrating the bouncing behavior of a DEP ($\Phi = 50.1\%$) in the partial retraction regime at $V = 1.243$ m s^{-1}. Scale bar, 0.5 mm. **b** Morphological changes of an impacting droplet and a DEP over time at $V = 1.243$ m s^{-1}. Both D and H are normalized by D_0. **c** Evolution of the normalized contact radius (R_c/R_0) for the droplet and DEP at $V = 1.243$ m s^{-1}. Both exhibit linear retraction with a constant retraction velocity of V_r. The contact radius of the DEP abruptly decreases from R_{ct} (contact radius at takeoff) to zero, indicating the partial retraction. **d** Dependence of the particle takeoff velocity (V_p) and liquid retraction velocity (V_r) on the impact velocity (V). V_r aligns with V_p. **e** Plot of R_{ct}/R_{cm} against V for the DEP. R_{cm} indicates the maximum contact radius. The normalized R_{ct} decreases almost linearly with increasing impact velocity V, suggesting a gradual increase in the length of liquid retraction. **f** Dependence of the contact time of the DEP on the impact velocity, with $t_c \propto V$.

https://doi.org/10.1038/s41467-024-54288-w

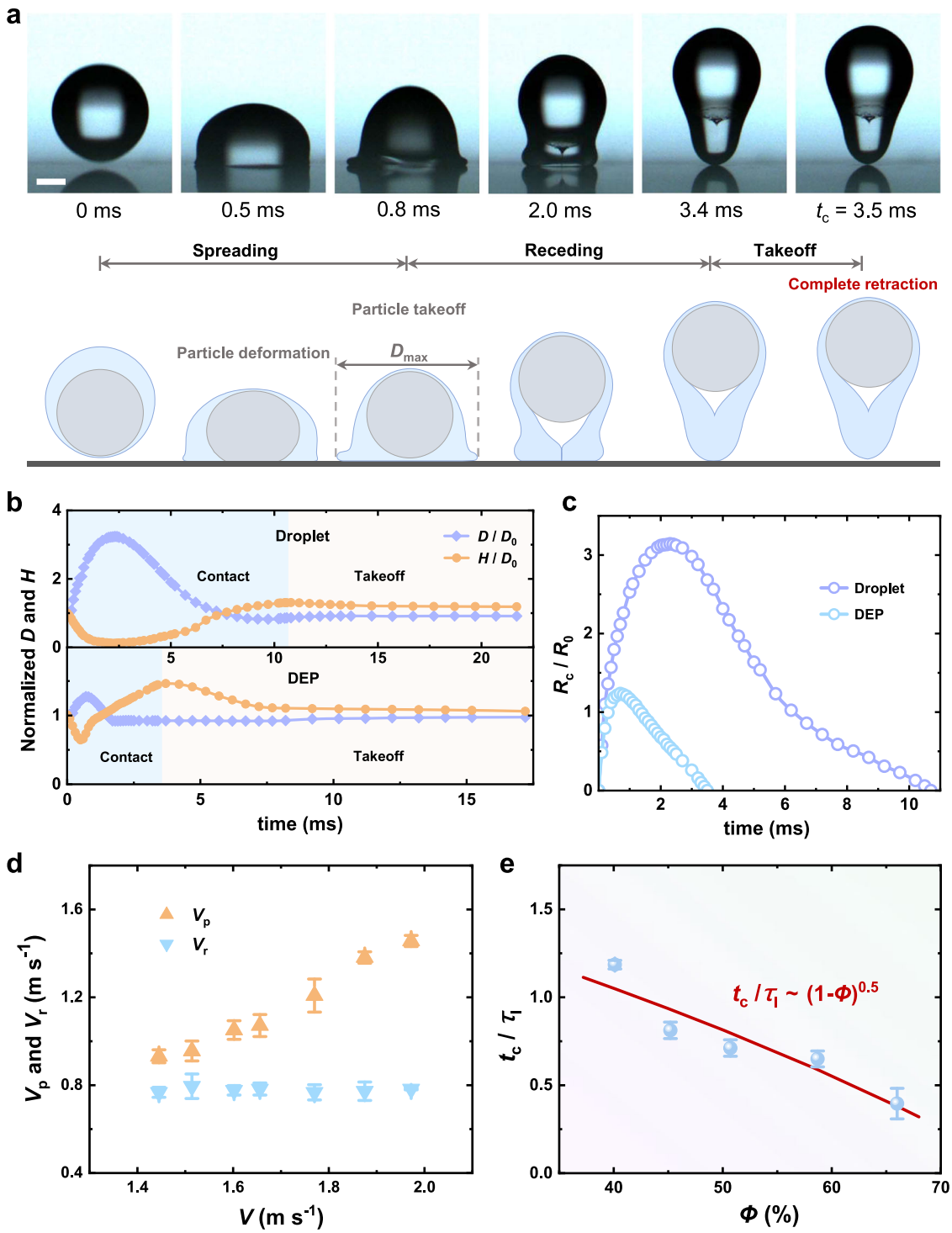

Fig. 5 | Complete retraction of DEP. a Snapshots and schematics illustrating DEP (Φ = 50.1%) bouncing in the complete retraction regime at V = 1.770 m s^{-1}. Scale bar, 0.5 mm. **b** Morphological variations of a droplet and a DEP over time at V = 1.770 m s^{-1}. Both D and H are normalized by D_0. **c** Evolution of the contact radius (R_c, normalized by R_0) for a droplet and a DEP at V = 1.770 m s^{-1}. **d** Dependence of the particle takeoff velocity (V_p) and liquid retraction velocity (V_r) on the impact velocity (V) with V_r deviating from V_p. **e** Dimensionless contact time of DEP with varying volume fractions Φ in the complete retraction regime. The fitting curve corresponds to the theoretical prediction in Eq. (2).

The transition from the partial retraction to the complete retraction regime is characterized by the decoupling of motion between the particle and the droplet shell. For this condition to be met, the takeoff kinetics of the particle ($\sim \rho_p V_p^2$) must dominate over the viscous forces exerted by the droplet shell [$\sim \mu V_p/(R_0 - R_p)$], leading to $\rho_p V_p^2 \sim \mu V_p/(R_0 - R_p) \sim \mu V_p(1-\Phi^{1/3})^{-1}/R_0$, where $R_p = \Phi^{1/3} R_0$. This scaling argument predicts a critical takeoff velocity (V_{pc}) of the particle, $V_{pc} \sim \mu(1-\Phi^{1/3})^{-1}/\rho_p R_0$. Considering that the particle's takeoff velocity increases linearly with the impact velocity (Figs. 4d and 5d, and Supplementary Fig. 6c), another critical V_{c2} can be predicted for the transition between the partial and complete retraction regimes as $V_{c2} \sim V_{pc} \sim \mu(1-\Phi^{1/3})^{-1}/\rho_p R_0$ (Supplementary Fig. 12b). Using

V_{c2}, we can define another critical $We = 2\rho_l V_{c2}^2 R_0/\gamma$ for the regime transition:

$$We \sim (\rho_l/\rho_p)^2 Oh^2 (1 - \Phi^{1/3})^{-2} \quad (4)$$

with the Ohnesorge number defined as $Oh = \mu/\sqrt{\rho_l \gamma R_0}$.

Figure 6 illustrates the transition diagram of DEP impact in terms of We and Φ, corresponding to different bouncing behaviors observed experimentally. The two transition boundaries align well with the scaling laws established in Eqs. (3) and (4). Notably, DEP with low Φ values exhibits no bouncing behavior, likely due to significant energy dissipation from both particle deformation and liquid viscosity. As impact velocity increases, DEP may eventually bounce in the complete retraction regime; however, the no-bouncing regime and its transition to the complete retraction regime fall outside the scope of this study.

Discussion

Regulating the contact time of DEP would prove beneficial in various scenarios involving solid-liquid composite systems. A representative example is icing water droplets comprising an ice core and a water shell. As a proof-of-concept demonstration, we illustrate that an icing water droplet ($\Phi = 53.8\%$) swiftly detaches from the superhydrophobic surface after impact ($V = 1.280$ m/s), exhibiting solid-dominant bouncing behavior in the Hertz regime (Fig. 7a and Supplementary Movie 8). The contact time (t_c) of the icing droplet measures just 0.4 ms, resulting in a contact time ratio (t_c/τ) of 0.028 (with $\tau = 14.1$ ms). Both the liquid retraction regime and Hertz regime are successively observed for the bounce of icing water droplets by increasing volume fraction (Fig. 7a, Supplementary Fig. 13, and Supplementary Movie 8). Consequently, the contact time decreases with Φ and sharply reduces to a nearly constant value when Φ exceeds the critical threshold (~50%) characterizing the regime transition (Fig. 7b). It's noteworthy that even with a low Φ of 31.5%, the icing droplet demonstrates a contact time ratio of 1.2, still representing a substantial reduction of ~45% (Fig. 7b).

In real-world conditions, water-ice mixtures, such as sleet, can adhere to surfaces like aircraft wings, wind turbine blades, and power lines, posing safety and performance challenges. For instance, ice accumulation on wind turbine blades can reduce aerodynamic efficiency, decrease energy output, and cause blade overload or even failure. Our findings provide new insights into the impact dynamics of icing droplets and contact time reduction, which have significant implications for mitigating icing-related issues in these scenarios.

In conclusion, this work demonstrates a remarkable reduction in contact time through the strategic manipulation of droplet heterogeneity, exemplified by the design of DEP. The study delineates three distinct bouncing regimes, the Hertz regime, partial retraction regime, and complete retraction regime. These regimes can be effectively controlled by adjusting the particle volume fraction and Weber number. Notably, DEP showcases a substantially short contact time (Supplementary Fig. 14) in any of the three regimes. Theoretically, further reduction in contact time is feasible by elevating the impact velocity and particle's Young's modulus and/or by decreasing the radius and effective density of DEP, as predicted by Eq. (1). This discovery holds significant promise as a robust and effective strategy for minimizing contact time in various applications. Given the ubiquity of solid-liquid composite systems in natural and industrial processes, ranging from fluidized beds, icing droplets, and partially molten particles to unset concrete, 3D printing inks, and drug-delivery systems, the implications of this research are anticipated to be far-reaching.

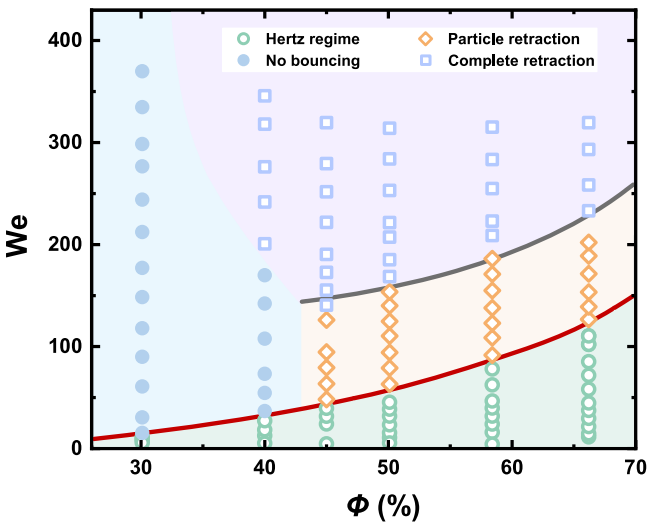

Fig. 6 | Transition diagram of the DEP impact. Symbols denote experimental results, while curves illustrate theoretical predictions derived from Eqs. (3) and (4) for the two transition boundaries, complete with fitting prefactors.

Methods

Fabrication of solid particles

PDMS particles were used unless otherwise specified. They were produced by solidifying the single-emulsion PDMS droplets generated by microfluidics. In the generation of emulsion droplets, the continuous

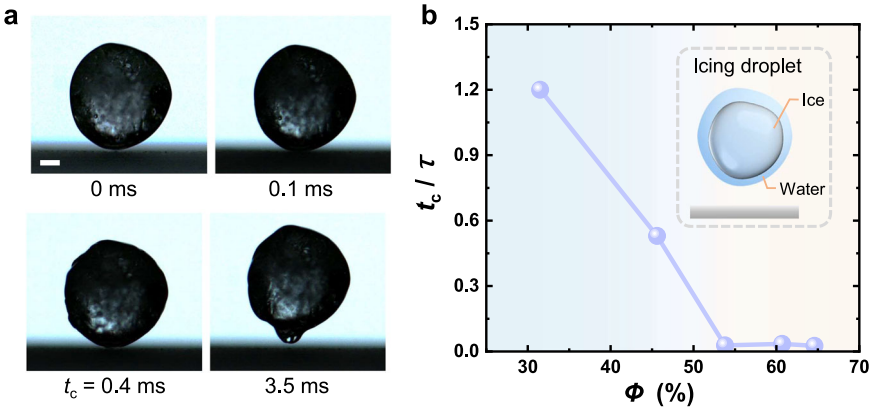

Fig. 7 | Contact time of icing water droplets. a Snapshots showcasing the bouncing dynamics of an icing droplet consisting of an ice core and a water shell during impact under the velocity of 1.280 m s^{-1}. The contact time t_c of icing droplet is 0.4 ms, and t_c/τ is 0.028. Scale bar, 1 mm. **b** The contact time ratio (t_c/τ) of icing droplets with different volume fractions of the ice core (Φ). Insert is the schematic of an icing droplet impacting on a solid surface.

phase fluid comprised a 5 wt% polyvinyl alcohol (PVA; molecular weight: 13000–23000, hydrolysis: 87-89%; Aldrich) aqueous solution, while the disperse phase fluid consisted of PDMS precursor (Sylgard 184), silicone oil, and curing agent. To reduce the viscosity of the dispersed solution and finely tune the mechanical strength of the resulting PDMS particles, low-viscosity silicone oil (0.65 cSt; Dow Corning) was introduced into the PDMS precursor in varying weight ratios, such as 1:0.5, 1:1, 1:2, 1:3, 1:4. Subsequently, the mixture was blended with the curing agent at a weight ratio of 10:1.

PDMS droplets of diverse sizes were generated in the dripping mode by adjusting fluid flow rates. Post-generation, the droplets underwent polymerization, transforming into solid particles through incubation in an oven set at 80 °C for 2 hours. To ensure the complete removal of residual PVA from the surface of PDMS particles, the resulting particles underwent a washing process with distilled water (4 to 5 times) followed by drying. The produced particles were meticulously examined for their degree of sphericity and size (Supplementary Fig. 1) under an optical microscope (Nikon ECLIPSE Ts2).

Hydrogel particles were synthesized by photopolymerizing water-in-oil emulsions. To produce emulsions using microfluidic technology, the dispersed phase liquid consisted of acrylamide (10 wt% or 30 wt%, Macklin), N,N′-methylenebisacrylamide (0.5 wt% or 3 wt%, Aladdin), and 2-Hydroxy-4′-(2-hydroxyethoxy)-2-methylpropiophenone (0.5 wt% or 2 wt%, Sigma), while the continuous phase liquid was silicone oil (0.65 cSt; Dow Corning). Aqueous droplets were generated in the dripping mode to ensure high uniformity. The collected emulsions were cured under an ultraviolet lamp for 0.5 hours to solidify aqueous droplets into hydrogel particles. Subsequently, the produced hydrogel particles were washed and stored in distilled water for future use.

Glass particles (Yingxu Chemical Machinery, Shanghai Co., Ltd.) were cleaned in an ultrasonic bath for 30 minutes using ethanol and acetone sequentially. After thorough rinsing with pure water, the particles were dried and stored for future use.

Generation of DEP

The core-shell DEP was produced using a microfluidic chip (Supplementary Fig. 15). A solid particle was positioned at the outlet of the microfluidic needle and adhered to the outlet by capillary forces. The shell liquid was expelled from the needle using a syringe pump (Longer Pump, LSP01-1A) at flow rates ranging from 0.5 mL h^{-1} to 3 mL h^{-1}. The vanishing contact angle between the particle and the liquid resulted in the complete encapsulation of the particle by the droplet shell, forming a DEP with a core-shell structure. The volume fraction of the particle could be adjusted by altering the particle size and the diameter of the needle (ranging from 0.16 mm to 0.34 mm to manipulate the DEP size). Four types of core-shell DEP were used in experiments: PDMS particles encapsulated in silicone oil (20 cSt; Dow Corning), glass particles encapsulated in silicone oil, polyacrylamide hydrogel particles (synthesized from 30 wt% monomer with a density of $\rho_p = 1190.5\ kg\ m^{-3}$) encapsulated in an aqueous solution of 75 wt% glycerol ($\rho_l = 1183.8\ kg\ m^{-3}$), and polyacrylamide hydrogel particles (synthesized from 10 wt% monomer with $\rho_p = 1023.4\ kg\ m^{-3}$) encapsulated in an aqueous solution of 38.6 wt% glycerol ($\rho_l = 1086.9\ kg\ m^{-3}$). A Janus structure was fabricated by combining a PDMS particle with a water droplet.

Generation of icing water droplets

The icing water droplets were formed from ice particles. At room conditions (Temperature of 26.6 °C and relative humidity of 57%), the melting of ice particles resulted in the formation of a water shell encapsulating the ice core. By controlling the melting time, icing droplets with varying volume fractions of the ice core were produced. These droplets were subsequently released from a height of 83.5 mm to conduct impact experiments. The mass of the icing droplet was measured as M_d, and that of the ice core was M_i. Using these values, the volume fraction of the ice core was determined as $\Phi = [1 + \left(\frac{M_d}{M_i} - 1\right)\frac{\rho_p}{\rho_l}]^{-1}$, where ρ_p and ρ_l represent the density of the ice particle and liquid water, respectively.

Fabrication of super-repellent surfaces

Superamphiphobic and superhydrophobic surfaces were utilized in experiments, with the former employed for DEPs containing PDMS and hydrogel particles, while the latter was used for water-PDMS Janus droplets and DEPs containing ice particles.

The fabrication of superamphiphobic surfaces followed the methodology detailed in our previous study[11]. Initially, a superamphiphobic suspension was synthesized. At 60 °C, 15 mL of ammonia (28-30%, Aladdin) was added to 45 mL of ethanol while stirring at 500 rounds per minute (RPM). Subsequently, 2 mL of tetraethyl orthosilicate (>99%, Macklin) was gradually introduced drop by drop into the solution. Once the solution turned opaque, 0.1 mL of 1H,1H,2H,2H-perfluorodecyltriethoxysilane (>98.0%, Aladdin) was added to the mixture. Approximately 24 hours were required for the reaction to complete, yielding a suspension containing superamphiphobic silica nanoparticles. Subsequently, the superamphiphobic suspension was applied to a glass substrate. This involved slowly depositing 1 mL of the suspension onto a glass slide (2.5 cm × 2.5 cm), followed by incubation in a drying oven at 50 °C for 50 minutes. This process ensured the uniform coating of fluorinated silica nanoparticles on the glass substrate, forming a superamphiphobic coating. The coating morphology was examined by scanning electron microscopy (SEM, FEI Quanta FEG 450).

The superhydrophobic coating solution was prepared using an aerosol suspension and an epoxy adhesive. First, 1 g of aerosol (EVONIK) was dissolved in 30 mL of ethanol and stirred at 600 rounds per minute (RPM) for 30 minutes to form a uniform suspension. Meanwhile, 2 g of epoxy resin (Macklin) was dissolved in 5 mL of ethanol through ultrasonic oscillation, producing a transparent solution. The curing agent for the epoxy was synthesized by mixing 1.07 mL of heptafluorobutyric acid (>99.5%, Aladdin) and 1.14 mL of N-[3-(trimethoxysilyl)propyl] ethylenediamine (>95%, Aladdin) in 20 mL of distilled water, followed by stirring for 15 minutes. The mixture was then heated at 120 °C to evaporate the water, resulting in a yellow colloidal curing agent, to which 5 mL of ethanol was added under stirring to form the final curing agent solution. The aerosol suspension, epoxy solution, and curing agent solution were then mixed, and 0.3 mL of 1H,1H,2H,2H-perfluorodecyltriethoxysilane (>98.0%, Aladdin) was added. This mixture was stirred for 1 hour to generate a superhydrophobic suspension. Subsequently, 3 mL of the suspension was sprayed onto a glass slide (2.5 cm × 7.5 cm), which was then baked at 120 °C for 5 hours to ensure a uniform and robust superhydrophobic coating with excellent water-repellency.

Impact experiments

The produced DEP was released from the outlet of the needle, allowing it to fall freely and impact directly onto the superamphiphobic, superhydrophobic, glass, aluminum, and PTFE surfaces. In control experiments, elastic particles or liquid droplets were similarly released directly from the needle to complete the impact process. To manipulate the impact velocity, adjustments were made by varying the release height. A high-speed camera (Fastcam Mini UX-100, Photron), equipped with an optical lens, was employed to capture the impact process of the different systems at a rate ranging between 8,000 to 40,000 frames per second (fps). Subsequently, the recorded videos were analyzed using ImageJ (National Institutes of Health). The error bars represent the standard deviations calculated from three to ten replicate experiments.

Characterization

The mechanical properties of elastic solids with different compositions were tested using PDMS strips by a tensile testing machine (Tian Yuan Test Instrument, TY8000-A). Young's modulus E can be obtained by analyzing the measured stress-strain curves (Supplementary Fig. 8). The contact angle and surface tension of liquids were measured by a goniometer (Shanghai Zhongbin Technology CO., LTD, CSCIDC-350), and the viscosity of liquids was measured by a viscometer (Shanghai Yixin Scientific Instrument Co., LTD, NDJ-1S).

Data availability

The data that support the findings of this study are available from the corresponding authors. Source data are provided with this paper.

References

1. Worthington, A. M. On the forms assumed by drops of liquids falling vertically on a horizontal plate. *Proc. R. Soc. Lond.* **25**, 261–272 (1877).
2. Richard, D., Clanet, C. & Quéré, D. Contact time of a bouncing drop. *Nature* **417**, 811–811 (2002).
3. Arora, S. et al. Impact of beads and drops on a repellent solid surface: a unified description. *Phys. Rev. Lett.* **120**, 148003 (2018).
4. Blanken, N., Saleem, M. S., Thoraval, M.-J. & Antonini, C. Impact of compound drops: a perspective. *Curr. Opin. Colloid Interface Sci.* **51**, 101389 (2021).
5. Hertz, H. On the contact of elastic solids. *J. Reine Angew. Math* **92**, 156–171 (1882).
6. Jung, S., Tiwari, M. K., Doan, N. V. & Poulikakos, D. Mechanism of supercooled droplet freezing on surfaces. *Nat. Commun.* **3**, 615 (2012).
7. Lambley, H. et al. Freezing-induced wetting transitions on superhydrophobic surfaces. *Nat. Phys.* **19**, 649–655 (2023).
8. Haechler, I. et al. Transparent sunlight-activated antifogging metamaterials. *Nat. Nanotechnol.* **18**, 137–144 (2023).
9. Lu, Y. et al. Robust self-cleaning surfaces that function when exposed to either air or oil. *Science* **347**, 1132–1135 (2015).
10. Blossey, R. Self-cleaning surfaces-virtual realities. *Nat. Mater.* **2**, 301–306 (2003).
11. Zhou, Y., Zhang, C., Zhao, W., Wang, S. & Zhu, P. Suppression of hollow droplet rebound on super-repellent surfaces. *Nat. Commun.* **14**, 5386 (2023).
12. Li, Y. et al. A droplet-based electricity generator incorporating Kelvin water dropper with ultrahigh instantaneous power density. *Droplet* **3**, e91 (2024).
13. Xu, W. et al. A droplet-based electricity generator with high instantaneous power density. *Nature* **578**, 392–396 (2020).
14. Jiang, M. et al. Inhibiting the Leidenfrost effect above 1,000 °C for sustained thermal cooling. *Nature* **601**, 568–572 (2022).
15. Kumar, V., Fu, Q., Szeto, H. & Zhu, Y. Heat transfer during droplet impact on a cold superhydrophobic surface via interfacial thermal mapping. *Droplet* **3**, e124 (2024).
16. Zhu, P., Chen, C., Nandakumar, K. & Wang, L. Nonspecular reflection of droplets. *Small* **17**, 2006695 (2021).
17. Bhushan, B. & Her, E. K. Fabrication of superhydrophobic surfaces with high and low adhesion inspired from rose petal. *Langmuir* **26**, 8207–8217 (2010).
18. Zhu, P., Chen, R. & Wang, L. Topography-directed hot-water superrepellent surfaces. *Adv. Sci.* **6**, 1900798 (2019).
19. Biance, A.-L., Chevy, F., Clanet, C., Lagubeau, G. & Quéré, D. On the elasticity of an inertial liquid shock. *J. Fluid Mech.* **554**, 47–66 (2006).
20. Deng, X., Mammen, L., Butt, H.-J. & Vollmer, D. Candle soot as a template for a transparent robust superamphiphobic coating. *Science* **335**, 67–70 (2012).
21. Schutzius, T. M. et al. Spontaneous droplet trampolining on rigid superhydrophobic surfaces. *Nature* **527**, 82–85 (2015).
22. Josserand, C. & Thoroddsen, S. T. Drop impact on a solid surface. *Annu. Rev. Fluid Mech.* **48**, 365–391 (2016).
23. Yarin, A. L. Drop impact dynamics: splashing, spreading, receding, bouncing. *Annu. Rev. Fluid Mech.* **38**, 159–192 (2005).
24. Rayleigh, L. On the capillary phenomena of jets. *Proc. R. Soc. Lond.* **29**, 71–97 (1879).
25. Bird, J. C., Dhiman, R., Kwon, H.-M. & Varanasi, K. K. Reducing the contact time of a bouncing drop. *Nature* **503**, 385–388 (2013).
26. Gauthier, A., Symon, S., Clanet, C. & Quere, D. Water impacting on superhydrophobic macrotextures. *Nat. Commun.* **6**, 8001 (2015).
27. Chantelot, P. et al. Water ring-bouncing on repellent singularities. *Soft Matter* **14**, 2227–2233 (2018).
28. Regulagadda, K., Bakshi, S. & Das, S. K. Morphology of drop impact on a superhydrophobic surface with macro-structures. *Phys. Fluids* **29**, 082104 (2017).
29. Lin, D.-J., Wang, L., Wang, X.-D. & Yan, W.-M. Reduction in the contact time of impacting droplets by decorating a rectangular ridge on superhydrophobic surfaces. *Int. J. Heat Mass Transf.* **132**, 1105–1115 (2019).
30. Abolghasemibizaki, M., McMasters, R. L. & Mohammadi, R. Towards the shortest possible contact time: Droplet impact on cylindrical superhydrophobic surfaces structured with macro-scale features. *J. Colloid Interface Sci.* **521**, 17–23 (2018).
31. Liu, Y. et al. Pancake bouncing on superhydrophobic surfaces. *Nat. Phys.* **10**, 515–519 (2014).
32. Li, X., Ma, X. & Lan, Z. Dynamic behavior of the water droplet impact on a textured hydrophobic/superhydrophobic surface: the effect of the remaining liquid film arising on the pillars' tops on the contact time. *Langmuir* **26**, 4831–4838 (2010).
33. Lv, C., Hao, P., Zhang, X. & He, F. Drop impact upon superhydrophobic surfaces with regular and hierarchical roughness. *Appl. Phys. Lett.* **108**, 141602 (2016).
34. Song, J. et al. Robust superhydrophobic conical pillars from syringe needle shape to straight conical pillar shape for droplet pancake bouncing. *ACS Appl. Mater. Interfaces* **11**, 45345–45353 (2019).
35. Liu, Y., Andrew, M., Li, J., Yeomans, J. M. & Wang, Z. Symmetry breaking in drop bouncing on curved surfaces. *Nat. Commun.* **6**, 10034 (2015).
36. Lin, C. et al. Reducing droplet contact time and area by craterlike surface structure. *Phys. Rev. Fluid* **6**, 083602 (2021).
37. Han, J. et al. Contact time on curved superhydrophobic surfaces. *Phys. Rev. E* **101**, 043108 (2020).
38. Wang, L., Wang, R., Wang, J. & Wong, T.-S. Compact nanoscale textures reduce contact time of bouncing droplets. *Sci. Adv.* **6**, eabb2307 (2020).
39. Huang, L. et al. Drop impact on elastic superhydrophobic films: From pancake bouncing to saucer bouncing. *Mater. Lett.* **285**, 129076 (2021).
40. Ding, S. et al. Regulation of droplet rebound behavior with contact time control on a flexible and superhydrophobic film. *Langmuir* **38**, 2942–2953 (2022).
41. Weisensee, P. B. et al. Droplet impact on vibrating superhydrophobic surfaces. *Phys. Rev. Fluid* **2**, 103601 (2017).
42. Tao, R. et al. Rotating surfaces promote the shedding of droplets. *Research* **6**, 0023 (2023).

Acknowledgements

This research was funded by the Research Grants Council of Hong Kong (21213621, SRFS2223-1S01), National Natural Science Foundation of China (52303046), and Shenzhen Science and Technology Program (JCYJ20220530140812028).

Author contributions

P.Z. conceived and supervised the research. P.Z. and Y.L. designed the experiments. Y.L. performed the experiments. W.Z. and S.T. assisted in the fabrication of the superamphiphobic surfaces. Y.Z. and S.W. assisted in fabricating the microfluidic devices. W.Z., Y.Z., S.T., and Y.T.Z. helped with the experiments and measurements. P.Z. and Y.L. analyzed and interpreted the results. P.Z. performed the theoretical analysis. Z.W. evaluated the study and contributed valuable ideas. P.Z. and Y.L. wrote the manuscript. All the authors discussed the results and commented on the manuscript.

Competing interests

The authors declare no competing interests.

Additional information

Supplementary information The online version contains supplementary material available at https://doi.org/10.1038/s41467-024-54288-w.

Correspondence and requests for materials should be addressed to Zuankai Wang or Pingan Zhu.

Peer review information *Nature Communications* thanks Choongyeop Lee and Reza Mohammadi for their contribution to the peer review of this work. A peer review file is available.